Semiconductor Physics, Quantum Electronics & Optoelectronics, 2026. V. 29, No 2. P. 136-145.

Semiconductor physics

First-principles study of $XGeO_3$ (X = Zn, Cd): Semiconducting perovskites for optoelectronic and thermoelectric applications

A.U. Haq[1], M.N. Tabassam[1], N. Ahmed[2], A. Shahzad[3], J. Qu[1,*], S. Golovynskyi[1,*]

[1]*College of Physics and Optoelectronic Engineering, Shenzhen University, 518060 Shenzhen, China*
[2]*College of Civil and Transportation Engineering, Shenzhen University, 518060 Shenzhen, China*
[3]*College of Electronics and Information Engineering, Shenzhen University, 518060 Shenzhen, China*
[*]*Corresponding author e-mail: jlqu@szu.edu.cn; serge@szu.edu.cn*

Abstract. The structural, mechanical, electronic, thermodynamic, optical, and thermoelectric properties of zinc germanate ($ZnGeO_3$) and cadmium germanate ($CdGeO_3$) are theoretically predicted using first-principles calculations based on density functional theory (DFT). We examined the crystal and electronic band structures, as well as optical and thermoelectric properties. Both compounds have the perovskite structure with lattice parameters of 3.68 Å for $ZnGeO_3$ and 3.74 Å for $CdGeO_3$. The $ZnGeO_3$ is more stable, with a minimal energy of −15832.079 Ry *versus* −15832.062 Ry for $CdGeO_3$. The electronic band structure shows direct bandgaps of 2.8 eV for $ZnGeO_3$ and 3.1 eV for $CdGeO_3$, confirming their semiconducting nature. The calculated optical properties include the dielectric function and absorption coefficient. $CdGeO_3$ has higher absorption peaks within the UV range. Thermoelectric performance is moderate, with the figure of merit values of 0.53 for $ZnGeO_3$ and 0.59 for $CdGeO_3$ at room temperature. These compounds show promise for optoelectronic applications, while their thermoelectric efficiency remains limited.

Keywords: perovskite, DFT, first-principles calculations, electronic properties, optical properties, thermoelectric properties.

https://doi.org/10.15407/spqeo29.02.136
PACS 71.15.Mb, 72.15.Jf, 72.20.Pa, 78.20.-e

Manuscript received 23.08.25; revised version received 12.04.26; accepted for publication 10.06.26; published online 23.06.26.

1. Introduction

Given increasing global energy demand, the rapid depletion of natural resources, and their adverse environmental impacts, research into green, cost-effective, sustainable, and clean energy solutions has become crucial [1, 2]. Perovskite (ABY_3) is one of the most extensively studied materials in condensed matter physics, capable of accommodating a wide range of anions and most metallic ions from the periodic table [3, 4].

Unlike traditional silicon-based technologies, perovskites have recently garnered significant interest in the scientific community [5, 6]. They possess outstanding optoelectronic properties, including long charge carrier diffusion length, tunable bandgap (E_g), low recombination rate, high carrier mobility, broad absorption, and strong dielectric response [7]. These characteristics make them highly suitable for various applications, such as solar cells (SCs), light-emitting diodes (LEDs), photovoltaics, and solar-to-power energy conversion systems [8, 9].

The growing interest in perovskite SCs is driven by their exceptional performance and affordability as highly efficient photovoltaic systems [10]. Since their introduction in 2009, perovskite SCs have undergone rapid advancements, achieving efficiency levels exceeding 25%, which is on par with commercial silicon SCs [11, 12]. Moreover, ongoing research to enhance the material properties of perovskite SCs suggests a potential for even greater efficiency improvements in future [10, 13].

The quest for advanced functional materials has intensified the exploration of perovskite oxides. In particular, the focus is on optical and thermoelectric properties, which are pivotal for next-generation optoelectronic and energy-conversion technologies [14]. Zinc germanate ($ZnGeO_3$) and cadmium germanate ($CdGeO_3$) perovskites are promising candidates due to their inherent semiconductor behaviour and structural versatility. They offer promising applications in LEDs, laser diodes, and high-efficiency thermoelectric devices. Understanding their electronic and thermal responses at the atomic level is critical for tailoring their performance to these technologies [15].

Historically, first-principles calculations rooted in density functional theory (DFT) revolutionized materials science. It enabled accurate predictions of electronic, optical, and transport properties without empirical parameters [16]. DFT provides a framework to compute electronic band structure (EBS), density of states (DOS),

and optical spectra by solving the quantum mechanical equations governing electron interactions [17]. Incorporating advanced exchange-correlation functionals further enhances accuracy in predicting E_g and optical responses. These calculations eliminate reliance on experimental data, making them indispensable for exploring novel materials [18].

Seminal studies on analogous perovskites, such as $SrTiO_3$ and $BaTiO_3$, demonstrated DFT efficacy in guiding experimental synthesis. However, $ZnGeO_3$ and $CdGeO_3$ (specifically their combined optical and thermoelectric characteristics) remain unexplored, leaving gaps in utilizing their full technological potential [19]. Prior works have mainly focused on structural or electronic properties in isolation, neglecting the interplay between optoelectronic efficiency and thermal transport.

This study theoretically predicts the optical and thermoelectric properties of $ZnGeO_3$ and $CdGeO_3$. We employ first-principles simulations *via* the WIEN2k package to comprehensively analyze these materials. Our objectives include explaining their direct bandgap nature, optical absorption spectra, and thermoelectric efficiency metrics, such as the Seebeck coefficient (S), power factor (PF), and figure of merit (ZT). Computations utilize the full-potential linearized augmented plane wave (FP-LAPW) method to model EBSs. At the same time, optical properties are derived from the spectra of dielectric function (ε), refractive index (n), extinction coefficient (k), absorption coefficient (α), electric conductivity (σ), reflectivity (R), and optical loss (L). Thermoelectric parameters are evaluated at varying chemical potential (μ) and temperature (T). Anticipated outcomes include identifying $ZnGeO_3$ and $CdGeO_3$ as direct-bandgap semiconductors with strong optical absorption within the visible range alongside low lattice thermal conductivity (κ).

2. Computational methods

All calculations were performed using DFT-based first-principles methods, implemented through the WIEN2k software package. The exchange-correlation functional was treated within the local density approximation (LDA) and generalized gradient approximation (GGA) frameworks of Perdew, Burke, and Ernzerhof (PBE) [20]. Specifically, PBEsol was employed for solid-state calculations, and the modified Becke–Johnson potential (mBJ) was used in combination with PBEsol (PBEsol+mBJP) to calculate E_g and optical properties of the materials. It is important to note that the mBJ potential was designed by Tran–Blaha and modified by Becke–Johnson [20].

For structural optimization, we calculated the lattice constants corresponding to the system's minimum total energy. The total energy was computed as a function of unit cell volume, and the equilibrium geometry was determined by plotting the energy *versus* volume curve for $ZnGeO_3$ and $CdGeO_3$. The minimum energy configuration was selected for further calculations of EBS and partial density of states (PDOS) using PBEsol+mBJP. To obtain the optical properties of $ZnGeO_3$ and $CdGeO_3$, we calculated the dielectric function (ε), refractive index (n), extinction coefficient (k), absorption coefficient (α), conductivity (σ), reflectivity (R), and optical loss (L) using the same computational setup. For thermoelectric calculations, we determined the chemical potential (μ) at room temperature and the Seebeck coefficient (S), power factor (PF), and figure of merit (ZT) at the Fermi energy (E_F) [21, 22].

Given the sensitivity of molecular calculations to computational parameters, we conducted convergence studies to ensure that the results were well-converged with respect to key parameters, such as supercell sizes, k-point meshes, and k-grid geometries. Specifically, we varied the k-point grid density and supercell size to examine the stability of our results. The k-point grids were sampled with a Monkhorst–Pack mesh, and the convergence with respect to both k-point mesh size and supercell volume was assessed by comparing the computed total energies and electronic properties. The energy convergence criterion was set to 10^{-6} Ry, and the calculations were performed using a 6×6×6 k-point grid for the 1×1×1 supercell and a finer 8×8×8 grid for the larger supercells. The results showed that the chosen parameters provided stable and converged values for the electronic band structure, DOS, and optical properties. These convergence tests are consistent with the findings of Schwarz *et al*. [23], who discussed the importance of such studies when using the WIEN2k package for similar materials. The influence of different k-point meshes and supercell sizes on the electronic properties was found to be minimal, confirming that the computational setup used in this study is reliable [24].

3. Results and discussion

3.1. Crystal structure

The geometrical structural optimization for the three-dimensional crystal $XGeO_3$ (X = Zn, Cd) was first analyzed by GGA. Using DFT total energy calculations, Fig. 1a shows the energy-volume relationship for $ZnGeO_3$ and $CdGeO_3$. According to energy minima, the two compounds have the most stable forms when their volumes are at equilibrium [25]. The value of the equilibrium volume for $ZnGeO_3$ (~340 a.u.^{3}) is smaller than that of $CdGeO_3$ (~355 a.u.^{3}) because Zn^{2+} has a smaller ionic radius than Cd^{2+}. Compared to other solutions, the total energy for $ZnGeO_3$ is lower, showing it is more stable under the same conditions. Fig. 1b shows the atomic structure. The unit cell (1×1×1) shown in the diagram consists of 2 molecules and 15 atoms in each molecule. $ZnGeO_3$ and $CdGeO_3$ are perfectly in order in the structure with a face-shared pair of O atoms. The lattice parameters a_0 for $ZnGeO_3$ and $CdGeO_3$ are 3.68 and 3.74 Å, respectively. The arrangement of O atoms in the perovskite structure in the $XGeO_3$ (X = Zn, Cd) is distorted from an ideal cubic lattice, forming an orthorhombic structure (*e.g.*, *Pbnm*). The shared O-O distances in ZnO_6 and CdO_6 polyhedra are shorter for faces and longer for edges, while GeO_6 octahedra exhibit shorter bond lengths compared to those of other polyhedra. For $ZnGeO_3$, the perovskite phase is optimized [22].

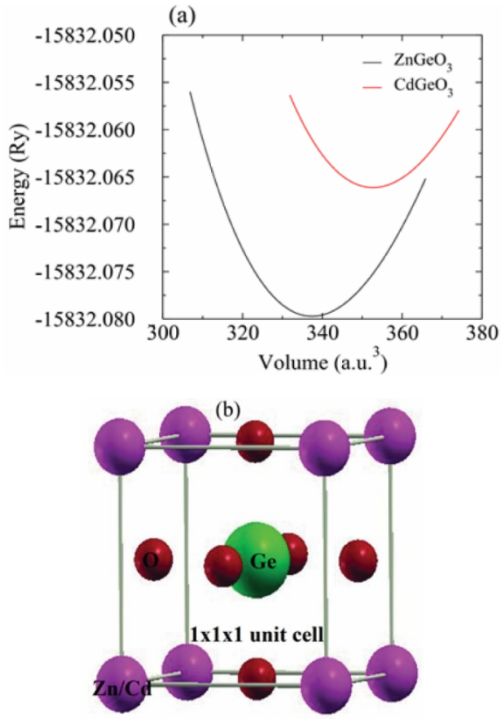

Fig. 1. (a) The energy *versus* volume plot and (b) crystal structure of $ZnGeO_3$ and $CdGeO_3$.

The energy *versus* volume (E–V, a.u.^{3}) plot (Fig. 1a) gives an approximation of the $XGeO_3$ compound that provides necessary information about thermodynamic properties like bulk modulus, which contributes to finding the thermal coefficient. Using the DFT approach, we investigated the free energy response of the crystal structure at various volumes of unit cells and obtained the E–V curve. Since we know that crystal structural properties give information about the stability of the material. The calculated total energy values plotted as a function of volume show that $ZnGeO_3$ is more stable compared to $CdGeO_3$ because of its smaller energy value. These energy values are used in the Murnaghan equation to get the mechanical properties mentioned above [26].

The E–V curve derivative gives the volume of the unit cell. The lattice parameter refers to unit cells $ZnGeO_3$ and $CdGeO_3$, which are 3.68 and 3.74 Å, respectively. The minimum energy (Ry) value is –15832.079 for $ZnGeO_3$, which makes it more stable, while –15832.062 for $CdGeO_3$, which has less stability [27]. We can find the value of bulk modulus B_0 (GPa) using the equation:

$$B = V_0\left[\frac{\partial^2 \phi}{\partial V^2}\right]. \qquad (1)$$

B_0 is 208 and 205 GPa for $ZnGeO_3$ and $CdGeO_3$, respectively (Table 1). In Eq. (1), V_0 is the maximum volume. We have approximated various properties based on DFT, which depend on the physical characteristics of the material, factors like C_{11}, C_{12}, C_{44}, G, E, Poisson's ratio (the ratio between B_0 and shear modulus, B_0/G), lattice constant, tolerance factor, anisotropy, *etc*. (Table 1).

Table 1. The calculated values of lattice parameters a_0 (Å), bulk modulus B_0 (GPa), tolerance factor t_{2G}, elastic constants C_{11}, C_{12}, and C_{44} (GPa), Poisson's ratio, the ratio of bulk modulus and shear modulus B_0/G, and anisotropy factor for $ZnGeO_3$ and $CdGeO_3$ perovskite.

Parameters	$ZnGeO_3$	$CdGeO_3$
a_0 (Å)	3.68	3.74
B_0 (GPa)	208	205
t_{2G}	0.96	0.97
C_{11}(GPa)	327	270
C_{12} (GPa)	154	177
C_{44} (GPa)	64	75
Poisson's ratio	0.35	0.36
B_0/G	2.91	3.37
Anisotropy factor	0.74	1.60

Table 2. Atoms with their respective electronic configurations.

Atoms in the crystal structure	Electronic configuration
Germanium, Ge–	$3d^{10}\ 4s^2\ 4p^2$
Cadmium, Cd–	$4d^{10}\ 5s^2$
Zinc, Zn–	$3d^{10}\ 4s^2$
Oxygen, O–	$2s^2\ 2p^4$

3.2. Electronic band structure

For any solid, EBS renders the most critical detail about energy levels [28]. It is observed that the electronic configuration of $XGeO_3$ is $(n-1)\ d^{10}\ ns^0$. Still, the potential used in the GGA approach is acquired for each atom and is shown in Table 2.

EBS of $ZnGeO_3$ and $CdGeO_3$ (Fig. 2) were calculated by the GGA code PBEsol+mBJ [29]. The energy values are modified so that the curves illustrate the upper portion of the valence band (VB) and the bottom of the conduction band (CB). The highest occupied energy state at 0 K is labelled as E_F.

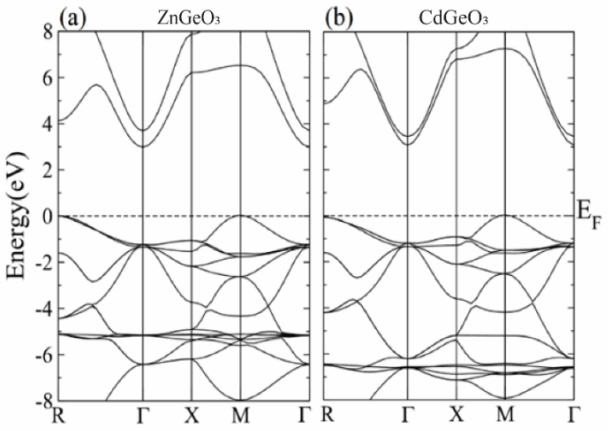

Fig. 2. The electronic band structures of (a) $ZnGeO_3$ and (b) $CdGeO_3$ calculated by PBEsol + mBJP.

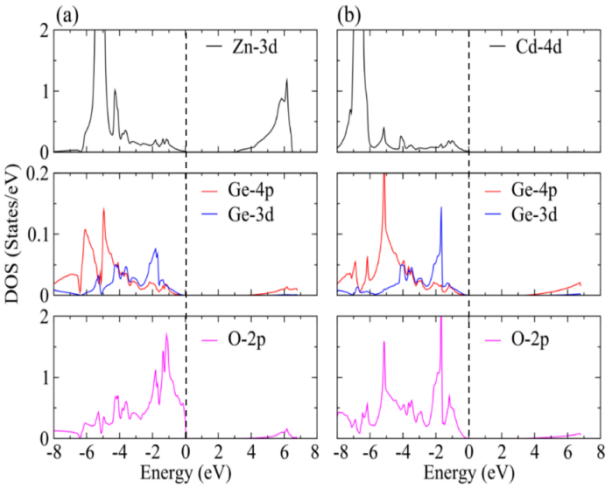

Fig. 3. Partial density of states (PDOS) for (a) $ZnGeO_3$ and (b) $CdGeO_3$ calculated using PBEsol + mBJP. The Fermi energy (E_F) is indicated by the dotted vertical lines at 0 eV.

In Fig. 2, EBS of $XGeO_3$ is similar to the Kohn–Sham EBS based on DFT [30]. The bottom (left), $ZnGeO_3$ and $CdGeO_3$ orthorhombic perovskites have a direct bandgap at the Γ-point within the GGA framework [21]. This gap is presented from the Γ indication in VB at the Γ-point in CB. It indicates anisotropy (variations in physical properties on different molecular axes) to small effective masses. In reciprocal space, such effective masses are inversely proportional to the band curvature at a particular point. Since the absolute form of the energy correlation functional is still unknown, we face some uncertainty in dealing with bandgaps by treating the compound properties based on LDA or GGA [28]. Besides this, with the help of certain approximations, we can predict the appropriate results very close to the experimental values.

In the GGA approach, the direct Γ-point transition for $ZnGeO_3$ is approximated to be 2.8 eV, while 3.1 eV for $CdGeO_3$; also, this transition is found to be very close to an indirect transition due to 2.8 eV for $ZnGeO_3$ [31]. Strong curvature in the uppermost VB for both $XGeO_3$ shows anisotropy. In CB, a similar feature is observed. This is because the order of maximum and minimum peaks is nearly similar for the lowest CB and depicts a direct bandgap. Even so, this E_g is narrower for $CdGeO_3$ than $ZnGeO_3$. Similarly, in Fig. 3, the Fermi energy (E_F) corresponds to 0 eV on the energy axis and is marked by a vertical line in both panels. Due to predicted E_g and Fermi level showing separation between valence and conduction band, both $XGeO_3$ (X = Zn, Cd) are proven semiconductors [31, 32].

Fig. 3 presents a contingent plot for PDOS per atomic species per orbital for $ZnGeO_3$ and $CdGeO_3$. In Fig. 3a, a sharp peak with an altitude of beyond two states/eV at about –5.9 eV energy, which grows from Zn 3*d* orbitals, is particularly present for Zn atoms. Some smaller peaks with heights ranging from 0.25 to 1.25 states/eV PDOS value at energies 3.9 to 6 eV in CB. While PDOS peaks come up from Ge, they are comparatively wider and found to be smaller than Zn because, in the outermost shell of Ge, there are only four electrons considered in computations. In comparison, Zn has only two valence electrons due to the filled 3*d* orbital. Ge contribution to PDOS has pulsating 4*p* and 3*d* peaks between 8.7 eV (*p*) and 8 to –0.1 eV (*d*), respectively [33]. In the end, each O atom has a valency of 6, which can generate deduce sets of VB, the first carry of 2*s* orbitals (no longer proven in Fig. 3) and the rest of all bands with O 2*p* orbital with energy range 8 to 0 eV with maximum 1.74 states/eV. So, we will say that for $ZnGeO_3$, the top of VB is dominated by the 2*p* contribution of O atoms. It is observed that the bottom of CB is developed by Ge 4*p* orbitals and Zn by way of 3*d* orbitals [34].

Fig. 3b presents the PDOS as per atomic species per orbital for $CdGeO_3$. The EBS donation of the Cd atom depicts the shrink peaks having an analogous height (beyond two states/eV) as that of the Zn atom in $ZnGeO_3$. However, here, energy variation is slight, about –6.8 eV, arising from Cd 4*d* orbital [35]. Smaller peaks in CB stem from Cd 5*s* orbitals between –4.5 to –1.0 eV and attain a maximum value of PDOS of ~0.35 states/eV [29]. However, the Ge atom contribution in PDOS from $CdGeO_3$ is relatively broader than Cd because 4 electrons are present in its outermost shell, while Cd has 12 electrons in its outermost shell. Ge atoms have peaks due to their 4*p* and 3*d* orbitals, which are alternatively from –7 to 6.9 eV (Ge 4*p*) and –8 to 0 eV (Ge 3*d*) [34]. Finally, as with $ZnGeO_3$, $CdGeO_3$ involves an O atom with 6 electrons in its outermost shell. Each atom produces peaks in VB with 2*p* orbital in the energy range from –8 to –0.1 eV with a maximum value of ~ 2 states/eV, and then a minor value is observed between 4.5 and 6.9 eV. This means some contribution is due to the *s* orbital, which is not shown in the above results [28].

The concept of charge transfer can be understood by the Quasi-Newtonian approximation, according to which the CB electrons and VB holes move under the effect of an applied magnetic field [36]. EBS provides the basis for finding the effective mass by the EBS curvature at high symmetry points in the Brillouin zone [37]. If curves show less curvature, the effective mass is large, and *vice versa* [38]. In the current work, the partial density of states (PDOS) of $ZnGeO_3$ (Fig. 3a) has variations in comparison to the findings of Hossain *et al*. [39], including the intensities of peaks as well as the structural features and location of the bandgap. These deviations can be explained by differing computational protocols: the current calculations are based on orbital-specific projections (Zn 3*d*, Ge 4*p*,3*d*, O 2*p*) and do not consider *s*-states, and also do not appear to use a bandgap correcting functional that would yield a bandgap of 3 eV or so. Conversely, the calculations by Hossain *et al.* [39] use the generalized gradient approximation (GGA-PBE) with *s* orbital contributions and normalize the PDOS on a unit cell basis. Hence, resulting in higher intensities and a reduced bandgap, close to 2.5 eV. These variations in methodology are common in the study of $ZnGeO_3$, *e.g*, the orthorhombic phase studied by Ozisik *et al*. [40] exhibits significantly different shapes of the elemental PDOS, whereas the rhombohedral phase studied by Zhang *et al*. (2013) has altered peak separation [41].

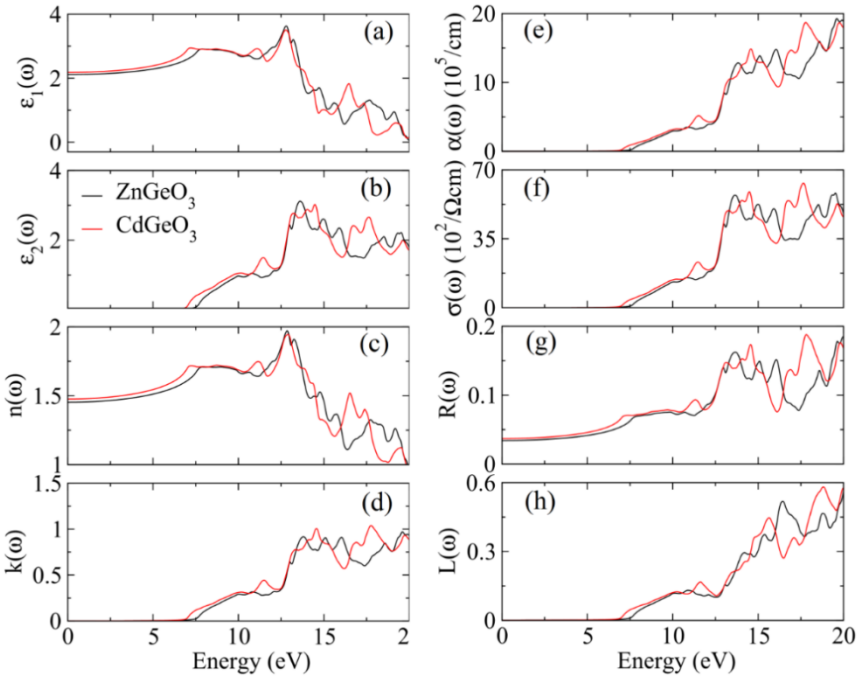

Fig. 4. Real ε_1 (a) and imaginary ε_2 (b) parts of dielectric constant, (c) refractive index *n*, (d) extinction coefficient *k*, (e) absorption coefficient α, (f) conductivity σ, (g) reflectivity *R*, and (h) optical loss *L* of $ZnGeO_3$ and $CdGeO_3$ calculated by PBEsol + mBJP.

The current results are qualitatively consistent with the previously reported work; the upper part of the valence band is dominated by the O_2 *p* orbitals, and the lower part of the valence band by the cation *d* 0 states, while the Ge *p*/*d* orbitals are at the conduction band minimum. These are electronic structure motifs that are repeated in the cubic [39], orthorhombic/trigonal [40], and rhombohedral phases. The increased bandgap calculated in the current study increases the accuracy of optical property calculations and alleviates the systematic underestimation problem of GGA functionals, which is emphasized in more recent works on perovskite using DFT.

3.3. Optical properties

The optical properties of a material depend on its ε and *n*. By DFT, we have calculated the various factors for $XGeO_3$ that act like its optical characteristics, as the ε constant (being a ground state property) of a material does not require any quasi-particle approximation. If we involve local field effects and self-energy correlation, ε might be affected [42]. As computations performed for EBS, here we performed a similar computational approach by using PBEsol + mBJP to find ε, *n*, *k*, α, σ, *R*, and *L* for both $ZnGeO_3$ and $CdGeO_3$, as shown in Fig. 4.

The real part of ε (ε_1) provides information about the ability to store charge. The real part of ε is plotted as a function of energy in Fig. 4a for $ZnGeO_3$ and $CdGeO_3$. The maxima of ε_1 for $ZnGeO_3$ are at 5.4, 10.25, 12.5, 15.1, 15.24, and 18.1 eV, and the highest peak is at 12 eV, while Lapp's highest peak value is observed for $CdGeO_3$. However, at ~16 eV, maxima exist only for $CdGeO_3$, while $ZnGeO_3$ shows minima at this energy state value. This shows the extinction of charge storage at this energy range [43].

The imaginary part of ε (ε_2) provides information regarding attenuation and absorption. Since the imaginary part ε_2 (Fig. 4b) is closely related to α, we are getting our search at α (Fig. 4e). The absorption peaks for $CdGeO_3$ are comparatively larger than for $ZnGeO_3$, indicating that light penetrates more in $CdGeO_3$ than $ZnGeO_3$ [44]. The first absorption peak found at ~11 eV is the smallest, while larger maxima were observed at 17.53 eV for $CdGeO_3$. Such peaks for $ZnGeO_3$ are from 13 to 19 eV. For both compounds, optical absorption rapidly increases above 11 eV due to oxygen 2*p* in the VB and Cd 5*s* / Zn 4*s* orbitals in the CBs. Because of the transition between valence states with O 2*p* to Ge 4*s* CB states, the first peak is minimal in the energy interval of 11 eV for $CdGeO_3$ and 10 eV for $ZnGeO_3$. We noticed a similar absorption E_g in all tops for both compounds. In Fig. 4d, *k* also describes peaks for different light absorption measures in a specified medium. By the application of the Kramers–Kronig transformation, ε_1 and ε_2 can be calculated using $\varepsilon_1(\omega) - i\varepsilon_2(\omega)$ [43].

Fig. 4c shows the *n* peaks. The value of *n* is almost the same for both materials within the energy range of 7.5 to 12.5 eV. This indicates that both materials similarly reduce the speed in a given medium within this energy range. However, above this energy, $CdGeO_3$ peaks are leading $ZnGeO_3$ [45].

It is the property of a material that correlates, at general frequencies, the current density to the electric field since it is based on ε [46]. Fig. 4f shows that at a given energy range from 7 to 10 eV, σ remains similar for both materials. However, σ of $CdGeO_3$ is greater above 10 eV than that of $ZnGeO_3$ since ε also has greater values for $CdGeO_3$. At the same time, the calculated *R* values are presented in Fig. 4g.

Table 3. The calculated room temperature values of electrical conductivity (σ), thermal conductivity (κ), Seebeck coefficient (*S*), power factor (PF), and figure of merit (ZT) of $ZnGeO_3$ and $CdGeO_3$ perovskites.

Perovskites	σ (10^{18}/Ω·m·s)	κ (10^{14} W/m·K)	*S* (μV/K)	PF (10^{12} W/(m·K^2·s))	ZT
$ZnGeO_3$	21.7	2.35	137	0.41	0.53
$CdGeO_3$	12.08	1.70	166	0.33	0.59

Optical loss occurs when light creates electron-hole pairs but is reflected from the surface instead of being transmitted into the material [46]. This *L* is related to the material's conductivity and the incident light energy [47]. Fig. 4h represents the calculated *L*, where the peaks indicate that *L* is smaller for $ZnGeO_3$ from 2 to 12.5 eV.

3.4. Thermoelectric properties

The thermoelectric response of a material depends on its κ, *S*, PF, and ZT. If a compound has a significant value of *S* with smaller values of σ and κ as well, then it can be considered a good thermoelectric material [48]. This is because these values of *S*, σ, and κ give rise to a greater value of ZT as per the formulated expression given by

$$ZT = \left(S^2/\rho\kappa\right)T. \qquad (2)$$

ZT should be greater than unity for a good thermoelectric material. The computations performed for $ZnGeO_3$ and $CdGeO_3$ based on DFT for σ and κ at varying μ (at room *T*), and *T* (at E_F) are shown in Fig. 5. The dependence of σ (Fig. 5a) upon μ (for both $ZnGeO_3$ and $CdGeO_3$) manifests that both compounds show maximum values of σ within the range –0.1 to 0 eV potential at room *T*. However, extreme peaks were observed at –0.035 and –0.04 eV for $CdGeO_3$ and $ZnGeO_3$, respectively. Both materials show zero conductivity within the μ range from 0 to 0.22 eV. It can be concluded that these materials seem to give beneficial thermoelectric responses in this potential range, but σ again increases from 0.23 to 0.3 eV almost equally [49, 50].

While at a smaller scale (along vertical) variation in σ (range 0…$0.4\cdot10^{20}$ 1/Ω·m·s) plotted against Fermi *T* (Fig. 5b), it is very clear that at 0 K, $CdGeO_3$ has σ close to 0.07 eV while $ZnGeO_3$ shows a larger value that is 0.17 eV. Above 0 K, σ increases linearly with *T*, indicating the semiconducting nature of perovskites $XGeO_3$.

The κ variation *versus* μ (Fig. 5c) is in an almost similar pattern to that of σ for both perovskites. However, the parabolic curve indicates that measures of κ increase with *T* rise (Fig. 5d). The gap between the two curves shows that κ for $CdGeO_3$ is smaller than $ZnGeO_3$. The computation results obtained from PBEsol + mBJP are tabulated in Table 3.

Results shown in Fig. 6a depict *S versus* μ and PF *versus* *T* at E_F. Two peaks are observed at different potential measures. Maxima occur (with a minor shift in peak position) at 0.07 eV with heights of $3\cdot10^3$ μV/K for both $ZnGeO_3$ and $CdGeO_3$, and then it drops suddenly at 0.16 eV for $ZnGeO_3$ and 0.17 eV for $CdGeO_3$. In Fig. 6b, PF is plotted as a function of *T* at E_F. The curve for $CdGeO_3$ increases sharply from 0 to 260 K and then constantly increases, but for $ZnGeO_3$, the curve increases almost constantly. The amplitude of the Seebeck-coefficient curve possesses a positive slope, a signature of an *n*-type material. PF is defined to be equal to σS^2. Usually, the literature shows that high-performance thermoelectric compounds usually have PF values within the range of 0.8…2.5 W·m^{-1}·K^{-1}. Figs. 6c, 6d represent PF plotted *versus* μ (at room *T*) and *T* (at E_F) for $ZnGeO_3$ and $CdGeO_3$ [51]. Fig. 6c shows different peaks for PF

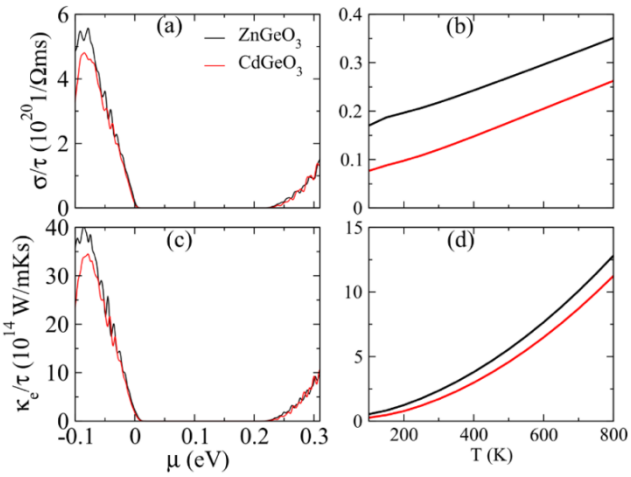

Fig. 5. Electrical conductivity σ (a, b) and thermal conductivity κ (c, d) *versus* chemical potential μ (at room temperature) and temperature *T* (at Fermi energy, E_F) for $ZnGeO_3$ and $CdGeO_3$.

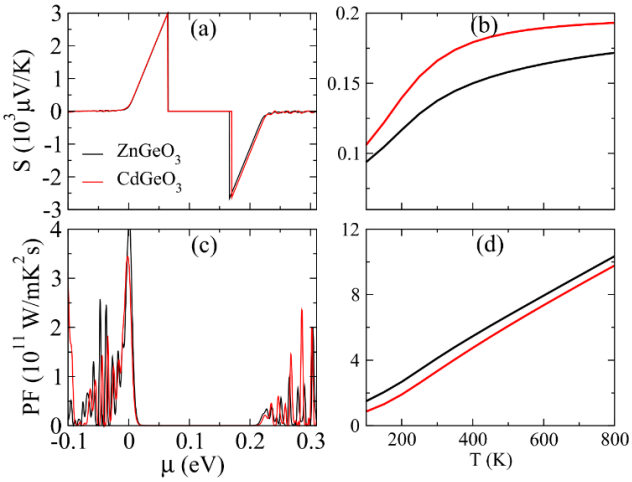

Fig. 6. (a, b) Seebeck coefficient *S* and (c, d) power factor PF plotted *versus* chemical potential μ (at room temperature) and temperature *T* (at Fermi energy, E_F) for $ZnGeO_3$ and $CdGeO_3$.

at the potential range –0.1…0.01 eV. Perovskites are promising thermo-electric materials, as predicted by the significant kinks at zero energy for given materials.

Suppose the potential increased further, then some peaks were observed at a potential range of 0.21 to 0.29 eV. This is consistent with experimental values. PF rises linearly with T (Fig. 6d). This can be attributed to the gap observed in curves for $CdGeO_3$ and $ZnGeO_3$ [52]. The calculated PFs from our computational results are given in Table 3.

4. Conclusions

The first-principles calculations for optical and thermo-electric properties of $XGeO_3$ (X = Zn, Cd) compounds were performed additionally to geometry optimization, EBS, DOS, PDOS, *etc*. GGA does all computations under PBEsol + mBJP. By the structural analysis of $XGeO_3$, a_0 was determined to be 3.68 Å for $ZnGeO_3$ and 3.74 Å for $CdGeO_3$. The E_g values obtained for $ZnGeO_3$ and $CdGeO_3$ show that they have a direct bandgap at the Γ-point in the limit of GGA computation. Therefore, the predicted E_g indicates that $XGeO_3$ (X = Zn, Cd) has a semiconductor nature. EBS provides the basis for finding the effective mass by the EBS curvature at significant symmetry points. A smaller curvature found in EBS gives the large effective mass of perovskites. DFT analysis proves that the VB is dominated by Zn/Cd *d*-orbitals and O 2*p* orbitals, while the lowest CB energy arises from Ge *p*/*d* orbitals.

The predicted optical properties declare that $XGeO_3$ is desirable for optoelectronic devices. $ZnGeO_3$ reduces the speed of light more than $CdGeO_3$ (due to its greater refractive-index peaks). Within the range 7…10 eV, σ remains almost the same for both materials, but above 10 eV, σ of $CdGeO_3$ is greater than that of $ZnGeO_3$ since ε also has greater values for $CdGeO_3$. Also, κ for $CdGeO_3$ is smaller than that of $ZnGeO_3$. Conversely, L is smaller for $ZnGeO_3$ within the range of 7.2 to 12.5 eV, whereas it was found to be greater at 16.5 eV than that of $CdGeO_3$. The values obtained for S and ZT indicate that both materials are good thermoelectric materials, but are not suitable for high-performance thermoelectric devices since they have positive values of ZT but less than unity. The amplitude of the S curve has a positive slope, which is a sign of an *n*-type material. Specifically, the quantitative variations in the calculated DOS/PDOS of $ZnGeO_3$ reflect the quantitative variations in exchange-correlation functional, orbital-projection schemes and normalization procedures but still the qualitative electronic features, including dominance of the O-2*p* in the valence band, the contribution of cation *p*/*d* to the conduction band, and the semiconducting nature are consistent with the previously reported theoretical and experimental trends, supporting the validity of the present optical and thermoelectric predictions.

Acknowledgements

This work was supported in part by the National Natural Science Foundation of China (62074103).

Declaration of Competing Interest

The authors declare that they have no known competing financial interests or personal relationships that could have appeared to influence the work reported in this paper.

References

1. Mitra S., Pak Y., Xin B. *et al.* Solar-blind self-powered photodetector using solution-processed amorphous core–shell gallium oxide nanoparticles. *ACS Appl. Mater. Interfaces.* 2019. **11**. P. 38921–38928. https://doi.org/10.1021/acsami.9b11694.
2. Riaz K., Drissi N., Abdalla S. *et al.* Computational exploration of structural, elastic, optoelectronic and magnetic properties of A_2YHgCl_6 (A = Cs, K) using enhanced computational techniques. *J. Inorg. Organomet. Polym. Mater.* 2025. **35**. P. 5363–5376. https://doi.org/10.1007/s10904-025-03594-x.
3. Khattak S.A., Abohashrh M., Ahmad I. *et al.* Investigation of structural, mechanical, optoelectronic, and thermoelectric properties of $BaXF_3$ (X = Co, Ir) fluoro-perovskites: promising materials for opto-electronic and thermoelectric applications. *ACS Omega.* 2023. **8**. P. 5274–5284. https://doi.org/10.1021/acsomega.2c05845.
4. Belyaev A., Maksimenko Z., Golovynskyi S. *et al.* Semiconductor nanomaterials for optoelectronics and the SPQEO. *SPQEO.* 2025. **28**. P. 004–009. https://doi.org/10.15407/spqeo28.01.004.
5. Chouhan L., Ghimire S., Subrahmanyam C. *et al.* Synthesis, optoelectronic properties and applications of halide perovskites. *Chem. Soc. Rev.* 2020. **49**. P. 2869–2885. https://doi.org/10.1039/C9CS00848A.
6. Zhang W., Eperon G.E., Snaith H.J. Metal halide perovskites for energy applications. *Nat. Energy.* 2016. **1**. P. 16048. https://doi.org/10.1038/nenergy.2016.48.
7. Rabhi S., Sekar K., Kalna K. *et al.* Enhancing perovskite solar cell performance through PbI_2 *in situ* passivation using a one-step process: experimental insights and simulations. *RSC Adv.* 2024. **14**. P. 34051–34065. https://doi.org/10.1039/D4RA06193D.
8. Ramasamy P., Lim D.-H., Kim B. *et al.* All-inorganic cesium lead halide perovskite nanocrystals for photodetector applications. *Chem. Commun.* 2016. **52**. P. 2067–2070. https://doi.org/10.1039/C5CC08643D.
9. Xiao Z., Yan Y. Progress in theoretical study of metal halide perovskite solar cell materials. *Adv. Energy Mater.* 2017. **7**. P. 1701136. https://doi.org/10.1002/aenm.201701136.
10. Magliano E., Di Giacomo F., Sathy H.R. *et al.* Solution-processed metal-oxide nanoparticles to prevent the sputtering damage in perovskite/silicon tandem solar cells. *ACS Appl. Mater. Interfaces.* 2025. **17**. P. 17599. https://doi.org/10.1021/acsami.5c00090.
11. Wolff C.M., Caprioglio P., Stolterfoht M. *et al.* Nonradiative recombination in perovskite solar cells: the role of interfaces. *Adv. Mater.* 2019. **31**. P. 1902762. https://doi.org/10.1002/adma.201902762.

12. Yang W.S., Park B.-W., Jung E.H. *et al.* Iodide management in formamidinium-lead-halide–based perovskite layers for efficient solar cells. *Science.* 2017. **356**. P. 1376–1379. https://doi.org/10.1126/science.aan2301.
13. Ahmad T.S., Ehsan N., Liaqat M. *et al.* Optoelectronic and thermoelectric analysis of halide stable double perovskite Rb_2TlSbX_6 (X = Cl, Br, I) via DFT calculations. *Results Phys.* 2024. **63**. P. 107885. https://doi.org/10.1016/j.rinp.2024.107885.
14. Prabhu M.., Kumar B.M., Ahilan A. Slime mould algorithm based fuzzy linear CFO estimation in wireless sensor networks. *IETE J. Res.* 2024. **70**. P. 3407–3417. https://doi.org/10.1080/03772063.2023.2194279.
15. Senden T., van Dijk-Moes R., Meijerink A. *et al.* Quenching of the red Mn^{4+} luminescence in Mn^{4+}-doped fluoride LED phosphors. *Light Sci. Appl.* 2018. **7**. P. 8. https://doi.org/10.1038/s41377-018-0013-1.
16. Bartolotti L.J., Flurchick K. An introduction to density functional theory. *Rev. Comput. Chem.* 1996. P. 187–216. https://doi.org/10.1002/9780470125847.ch4.
17. Tabassam M.N., Shahzad A., Almunyif A.A. *et al.* Structural, mechanical, electronic, optical, and thermoelectric properties of Sr_2XUO_6 (X = Cr, Dy): A first principles investigation for photovoltaic applications. *J. Phys. Chem. Solids.* 2025. **204**. P. 112770. https://doi.org/10.1016/j.jpcs.2025.112770.
18. Israr N., Jehangir M.A., Tighezza A.M. *et al.* The effect of PBEsol GGA and mBJ potentials on the structural, electronic, optical, elastic and thermoelectric properties of A_2BAuI_6 (A = K or Rb or Cs, B = Sc or Y). *Mater. Sci. Semicond. Process.* 2025. **186**. P. 109116. https://doi.org/10.1016/j.mssp.2024.109116.
19. Nawaz D., Parker O. Theoretical insights into strain-induced property modifications in inorganic perovskite Mg_3AsX_3: A computational analysis. *Comput. Anal.* 2025. https://doi.org/10.13140/RG.2.2.25915.94245.
20. Schwarz K., Blaha P., Madsen G.K. Electronic structure calculations of solids using the WIEN2k package for material sciences. *Comput. Phys. Commun.* 2002. **147**. P. 71–76. https://doi.org/10.1016/S0010-4655(02)00206-0.
21. Ghaithan H.M., Alahmed Z.A., Qaid S.M.H. *et al.* Structural, electronic, and optical properties of $CsPb(Br_{1-x}Cl_x)_3$ Perovskite: First-principles study with PBE–GGA and mBJ–GGA methods. *Materials.* 2020. **13**. P. 4944. https://doi.org/10.3390/ma13214944.
22. Manjón F.J., Errandonea D. Pressure-induced structural phase transitions in materials and earth sciences. *phys. status solidi (b).* 2009. **246**. P. 9–31. https://doi.org/10.1002/pssb.200844238.
23. Schwarz K., Blaha P., Trickey S.B. Electronic structure of solids with WIEN2k. *Mol. Phys.* 2010. **108**. P. 3147–3166. https://doi.org/10.1080/00268976.2010.506451.
24. Blaha P., Schwarz K., Tran F. *et al.* WIEN2k: An APW+lo program for calculating the properties of solid. *J. Chem. Phys.* 2020. **152**. P. 074101. https://doi.org/10.1063/1.5143061.
25. Barboza C., Henriques J., Albuquerque E. *et al.* Structural, electronic and optical properties of orthorhombic $CdGeO_3$ from first principles calculations. *J. Solid State Chem.* 2010. **183**. P. 437–443. https://doi.org/10.1016/j.jssc.2009.11.033.
26. Ross N.L., Leinenweber K. Single crystal structure refinement of high-pressure $ZnGeO_3$ ilmenite. *Z. Kristallogr.* 1990. **191**. P. 93–104. https://doi.org/10.1524/zkri.1990.191.14.93.
27. Weidner D.J., Hamaya N. Elastic properties of the olivine and spinel polymorphs of Mg_2GeO_4, and evaluation of elastic analogues. *Phys. Earth Planet. Inter.* 1983. **33**. P. 275–283. https://doi.org/10.1016/0031-9201(83)90045-6.
28. Borlido P., Schmidt J., Huran A.W. *et al.* Exchange-correlation functionals for band gaps of solids: Benchmark, reparametrization and machine learning. *NPJ Comput. Mater.* 2020. **6**. P. 96. https://https://doi.org/10.1038/s41524-020-00360-0.
29. Habib A., Husain M., Sajjad M. *et al.* Insight into the exemplary physical properties of Zn-based fluoroperovskite compounds $XZnF_3$ (X = Al, Cs, Ga, In) employing accurate GGA approach: A first-principles study. *Materials.* 2022. **15**. P. 2669. https://doi.org/10.3390/ma15072669.
30. Ghaithan H.M., Alahmed Z.A., Qaid S.M.H. *et al.* Density functional study of cubic, tetragonal, and orthorhombic $CsPbBr_3$ perovskite. *ACS Omega.* 2020. **5**. P. 7468–7480. https://doi.org/10.1021/acsomega.0c00197.
31. Yusa H., Akaogi M., Sata N. *et al.* High-pressure transformations of ilmenite to perovskite, and lithium niobate to perovskite in zinc germanate. *Phys. Chem. Miner.* 2006. **33**. P. 217–226. https://doi.org/10.1007/s00269-006-0070-5.
32. Karimi S., Esmaeili A. The performance of various GGA and LDA based mixed and improved exchange-correlation functionals for ZnO and ZnO:Mn: A first principles study. *Comput. Condens. Matter.* 2020. **25**. P. e00501. https://doi.org/10.1016/j.cocom.2020.e00501.
33. Ghaithan H.M., Alahmed Z.A., Qaid S.M.H. *et al.* Density functional theory analysis of structural, electronic, and optical properties of mixed-halide orthorhombic inorganic perovskites. *ACS Omega.* 2021. **6**. P. 30752-30761, https://doi.org/10.1021/acsomega.1c04806.
34. Satapathy S., Batouche M., Seddik T. *et al.* First principle study on structural, thermoelectric, and magnetic properties of cubic $CdCrO_3$ perovskites: A comprehensive analysis. *Crystals.* 2023. **13**. P. 1185. https://doi.org/10.3390/cryst13081185.
35. Zhang J., Xu B., Wang Y.-S. *et al.* First-principles investigation of the ferroelectric, piezoelectric and nonlinear optical properties of $LiNbO_3$-type $ZnTiO_3$. *Sci. Rep.* 2019. **9**. P. 17632. https://doi.org/10.1038/s41598-019-53986-6.
36. Chan M., Cuevas-Saavedra R., Chakraborty D. *et al.* A diagonally updated limited-memory quasi-Newton method for the weighted density

approximation. *Computation.* 2017. **5**. P. 42. https://doi.org/10.3390/computation5040042.
37. Hautier G., Miglio A., Ceder G. *et al.* Identification and design principles of low hole effective mass *p*-type transparent conducting oxides. *Nat. Commun.* 2013. **4**. P. 2292. https://doi.org/10.1038/ncomms3292.
38. Moskvin A. Charge transfer transitions and circular magnetooptics in ferrites. *Magnetochemistry.* 2022. **8**. P. 81. https://doi.org/10.3390/magnetochemistry8080081.
39. Hossain M.M., Al Mahmud A. Structural, elastic, electronic and optical properties of lead free $ZnMO_3$ (M = Ge, Sn) perovskites from first principles investigation. *Comput. Condens. Matter.* 2022. **32**. P. e00695. https://doi.org/10.1016/j.cocom.2022.e00695.
40. Ozisik H., Simsek S., Deligoz E. *et al.* Optical and electronic properties of orthorhombic and trigonal AXO_3 (A = Cd, Zn; X = Sn, Ge): First principle calculation. *Ferroelectrics.* 2016. **498**. P. 73–79. https://doi.org/10.1080/00150193.2016.1168207.
41. Zhang J., Xu B., Qin Z. *et al.* Ferroelectric and nonlinear optical properties of the $LiNbO_3$-type $ZnGeO_3$ from first-principles study. *J. Alloys Compd.* 2012. **514**. P. 113–119. https://doi.org/10.1016/j.jallcom.2011.11.017.
42. Abdullah D., Gupta D.C. Analyzing the structural, optoelectronic, and thermoelectric properties of $InGeX_3$ (X = Br) perovskites via DFT computations. *Sci. Rep.* 2024. **14**. P. 23575. https://doi.org/10.1038/s41598-024-72745-w.
43. Behera D., Mukherjee S.K. Optoelectronics and transport phenomena in Rb_2InBiX_6 (X = Cl, Br) compounds for renewable energy applications: A DFT insight. *Chemistry.* 2022. **4**. P. 1044–1059. https://doi.org/10.3390/chemistry4030071.
44. Calzolari A., Nardelli M.B. Dielectric properties and Raman spectra of ZnO from a first principles finite-differences/finite-fields approach. *Sci. Rep.* 2013. **3**. P. 2999. https://doi.org/10.1038/srep02999.
45. Farooq U., Israr N., Hassan B. *et al.* Unveiling the impact of 0–20 GPa hydrostatic pressure on the physical properties of (Cs_2HfCl_6) double perovskite. *Crystals.* 2025. **15**. P. 395. https://doi.org/10.3390/cryst15050395.
46. Ramanathan A.A. First principles investigation of the optoelectronic properties of molybdenum dinitride for optical sensing applications. *Chem. Proc.* 2021. **5**. P. 27. https://doi.org/10.3390/CSAC2021-10429.
47. Khan H., Sohail M., Arif M., Abodayeh K. Insight into the physical properties of fluoro-perovskites compounds of Tl-based $TlMF_3$ (M = Au, Ga) compounds studied for energy generation utilizing the TB-MBJ potential approximation approach. *Materials.* 2023. **16**. P. 686. https://doi.org/10.3390/ma1602068.
48. Sanin-Villa D. Recent developments in thermoelectric generation: A review. *Sustainability.* 2022. **14**. P. 16821. https://doi.org/10.3390/su142416821.
49. Peng Q., Ma X., Yang X. *et al.* Thermoelectric properties of $Mg_3(Bi,Sb)_2$ under finite temperatures and pressures: A first-principles study. *Nanomaterials.* 2024. **14**. P. 84. https://doi.org/10.3390/nano14010084.
50. Zhang Z.L., Yang W.Y., Wu B. *et al.* A Zn-doped Sb_2Te_3 flexible thin film with decoupled Seebeck coefficient and electrical conductivity via band engineering. *Chem. Sci.* 2025. **16**. P. 3638–3645. https://doi.org/10.1039/d4sc07793h.
51. Dey A., Sharma R., Dar S.A. *et al.* Cubic $PbGeO_3$ perovskite oxide: A compound with striking electronic, thermoelectric and optical properties, explored using DFT studies. *Comput. Condens. Matter.* 2021. **26**. P. e00532. https://doi.org/10.1016/j.cocom.2020.e00532.
52. Caillat T., Fleurial J.P., Borshchevsky A. Preparation and thermoelectric properties of semiconducting Zn_4Sb_3. *J. Phys. Chem. Solids.* 1997. **58**. P. 1119–1125. https://doi.org/10.1016/S0022-3697(96)00228-4.

Authors and CV

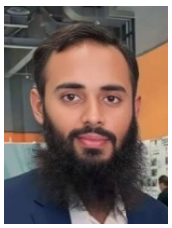

Anwar Ul Haq earned his Master's in Chemistry from the University of Agriculture, Faisalabad, in 2021. He is currently pursuing a PhD in Optoelectronic Engineering at Shenzhen University, China. His research centers on the synthesis of perovskite quantum dots and nanomaterials for biomedical imaging. His work integrates semiconductor physics, optics, and nanotechnology. He has authored over 7 publications, getting an H-index of 10. E-mail: anwarkabeer111@gmail.com, https://orcid.org/0000-0002-2788-4622

Muhammad Naeem Tabassam is a PhD candidate in Physics at Shenzhen University, China. He holds a Master's degree in Physics from the University of Lahore, Pakistan. His research focuses on Density Functional Theory (DFT), particularly the theoretical study of perovskite materials. He explores material-based sensors for advanced sensing applications. He has authored eight research papers in the field. https://orcid.org/0009-0004-4583-2609, e-mail: naeemtabassam@gmail.com

Naveed Ahmad is a PhD student at Shenzhen University, focusing on porous clay-based geopolymers and catalysts for wastewater treatment and energy applications. He has a strong background in chemistry and nanomaterials, including work on iron oxide nanoparticles, MXenes, and hybrid systems. His research spans 2D materials, photocatalysis, and advanced functional composites. Since 2018, he has contributed to multiple interdisciplinary projects.
E-mail: naveedahmad19137@gmail.com,
https://orcid.org/0000-0001-8812-6916

Amir Shahzad is a PhD candidate in Integrated Circuit Engineering at Shenzhen University, China. He holds a Master's in Power Electronics from Nanjing University of Science and Technology and a Bachelor's in Electrical Power Engineering from COMSATS University Islamabad. His research focuses on semi-conductor power devices (SiC, GaN), power converter design, and inverter topologies. He is also interested in smart energy systems and integrated circuits. E-mail: amirshahzad2024@email.szu.edu.cn

Junle Qu received his PhD in Physical Electronics from the Xi'an Institute of Optics and Precision Mechanics, Chinese Academy of Sciences in 1998. He is a chair professor of Optical Engineering at the Shenzhen University, China. His research interests include optoelectronics, nanomaterials, nonlinear optical microscopy, fluorescence imaging, superresolution optical imaging, and their applications in biomedicine. He has published over 700 scientific papers and holds over 90 issued patents, obtaining an H-index of 76. He is a senior member of SPIE and the Chinese Optical Society and an editor of several journals.
https://orcid.org/0000-0001-7833-4711

Sergii Golovynskyi defended his PhD thesis in Optics and Laser Physics in 2012 at the Taras Shevchenko National University of Kyiv, Ukraine. In 2012, he started his research career at the V. Lashkaryov Institute of Semiconductor Physics, NAS of Ukraine. Since 2016, he has been an associate researcher at Shenzhen University, China. His main research activity is in the fields of semiconductor physics and optics, spectroscopy, nanomaterials, and optoelectronics. Author of 90 scientific articles, obtaining an H-index of 24. He serves on the editorial board of several journals.
https://orcid.org/0000-0002-1864-976X

Authors' contributions

Ul Haq A.: conceptualization, investigation, data curation, formal analysis, visualization, writing original draft.
Tabassam M.N.: conceptualization, investigation, data curation, formal analysis, visualization, writing original draft.
Ahmed N.: formal analysis, writing – review & editing.
Shahzad A.: formal analysis, writing – review & editing.
Qu J.: resources, supervision, writing – review & editing.
Golovynskyi S.: formal analysis, visualization, supervision, writing – review & editing.

Дослідження $XGeO_3$ (X = Zn, Cd) на основі перших принципів: напівпровідникові перовскіти для оптоелектронних та термоелектричних застосувань

A.U. Haq, M.N. Tabassam, N. Ahmed, A. Shahzad, J. Qu, S. Golovynskyi

Анотація. Структурні, механічні, електронні, термодинамічні, оптичні та термоелектричні властивості германату цинку ($ZnGeO_3$) та германату кадмію ($CdGeO_3$) теоретично передбачені за допомогою розрахунків з перших принципів на основі теорії функціоналу густини (DFT). Ми дослідили кристалічну та електронну зонну структуру, а також оптичні та термоелектричні властивості. Обидві сполуки мають перовскітну структуру з параметрами решітки 3,68 Å для $ZnGeO_3$ та 3,74 Å для $CdGeO_3$. $ZnGeO_3$ є більш стабільним, з мінімальною енергією –15832,079 Ry проти –15832,062 Ry для $CdGeO_3$. Електронна зонна структура показує прямі заборонені зони 2,8 еВ для $ZnGeO_3$ та 3,1 еВ для $CdGeO_3$, що підтверджує їх напівпровідникову природу. Розраховані оптичні властивості містять діелектричну функцію та коефіцієнт поглинання. $CdGeO_3$ має вищі піки поглинання в УФ-діапазоні. Термоелектричні характеристики помірні, зі значеннями показника добротності 0,53 для $ZnGeO_3$ та 0,59 для $CdGeO_3$ за кімнатної температури. Ці сполуки є перспективними для електронних та оптоелектронних застосувань, хоча їхня термоелектрична ефективність залишається обмеженою.

Ключові слова: перовскіт, DFT, розрахунки з перших принципів, електронні властивості, оптичні властивості, термоелектричні властивості.